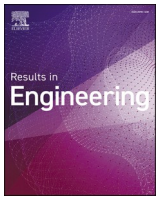
Results in Engineering 32 (2026) 113196



Contents lists available at ScienceDirect

Results in Engineering

journal homepage: www.sciencedirect.com/journal/results-in-engineering



Research paper

Ride comfort analysis of transient real world road signals through accurate frequency component identification

Oscar Montserrat Coll [a,*], Jon García-Barruetabeña [b]

[a] Virtual Development Center, Automotive Intelligence Center, Parque Empresarial Boroa, P2-A4, 48340 Amorebieta-Etxano, Bizkaia, Spain
[b] Department of Design Mechanical, Design and Industrial Management, Deusto University, Unibertsitate Etorbidea. 24, Bilbao, Bizkaia, 48007, Spain

ARTICLE INFO

Keywords:
Ride comfort
Non-stationary road excitation
Short-time analysis
Power spectral density
Parameter identification
Signal reconstruction
Vibration dose value (VDV)

ABSTRACT

This paper presents a ride-comfort strategy for non-stationary road excitations. Because real road inputs are transient, accurate identification of their frequency, amplitude, and damping components is essential for subsequent comfort assessment. The proposed methodology performs short-time analysis by combining autoregressive spectral estimation and power spectral density with a nonlinear error-minimization procedure to estimate the frequency components of the road signal, so precise comfort analysis can be executed. The approach is first validated on a controlled synthetic signal built from 15 sinusoids with predefined frequency, amplitude and damping values in different windows over a 10 s signal. In the synthetic validation case, the method recovered the imposed components with frequency errors below 0.5%, amplitude errors below 8%, damping errors within 5%, a mean absolute window-wise VDV error of 1.7%, and a maximum absolute VDV discrepancy of 5.8% across the nine analysis windows. These low errors indicate that the reconstructed signal preserves the event severity, supporting practical comfort comparison between road excitations. The coherence between original and reconstructed signals supports the reconstruction accuracy, with a minimum mean coherence of 0.91, while time-frequency trends are visualized with Campbell diagrams to track natural frequencies emerging within windows. Then, the proven methodology is applied to three non-stationary real world road measurements obtained from experiments. Based on the identified components, ride-comfort metrics are computed following ISO 2631-1. The resulting reconstruction-based representation of transient components enables comfort studies for virtual development of automotive systems under realistic time-varying excitations.

1. Introduction

Ride comfort has become a critical design target with the rise of electric and autonomous vehicles (AVs). In battery electric vehicles (BEVs), the reduction of powertrain-related vibration and acoustic masking increases occupants' sensitivity to road-induced, suspension-related and structurally transmitted vibrations. At the same time, automated driving shifts occupants towards a more passive role, making motion comfort a key acceptance factor. Recent surveys and noise, vibration and harshness (NVH) case studies report that ride comfort ranks alongside range for BEVs and strongly influences acceptance in AVs [1,2]. Consequently, identifying the specific causes of vibrations (even when they occur only for short time intervals) is essential for mitigation and virtual development. Related vibration-based approaches have also shown that vehicle response measurements can be exploited to infer pavement roughness in a practical and cost-effective manner, reinforcing the value of extracting road related information directly from measured vibration signals [3].

Ride comfort, although subjective, can be assessed with frequency-based models that relate vehicle vibration components to human perception. The low-frequency structural ranges commonly discussed in ride studies are considered (Ride 0.5–5 Hz, Shake 5–25 Hz, Harshness 25–80 Hz, and >80 Hz) [4–7], and comfort is quantified using the Vibration Dose Value (VDV) per ISO 2631-1 [5] because it integrates frequency-weighted magnitude and exposure duration, emphasizing short-duration peaks and shocks [6]. In this workflow, VDV is evaluated on a window-by-window basis.

Despite significant progress in accurate comfort predictions, three limitations persist: **(i)** most PSD-based studies assume stationary excitations, underrepresenting brief but perceptually important transients [8,9]; More recent PSD-based road characterisation studies remain highly valuable for describing surface roughness and generating

* Corresponding author.
E-mail addresses: o.montserrat@aicenter.eu (O. Montserrat Coll), jgarcia.barruetabena@deusto.es (J. García-Barruetabeña).

https://doi.org/10.1016/j.rineng.2026.113196
Received 22 April 2026; Received in revised form 25 June 2026; Accepted 24 September 2026
Available online 25 September 2026
2590-1230/© 2026 The Authors. Published by Elsevier B.V. This is an open access article under the CC BY license (http://creativecommons.org/licenses/by/4.0/).

representative virtual surfaces, but they are still not intended to resolve the time localisation of short transient events that dominate comfort perception [10]; **(ii)** Autoregressive (AR) approaches are rarely combined with comfort metrics, preventing a direct link between spectral findings and occupant perception [11,12]; **(iii)** simulator based works such as [13] demonstrate accurate replication of road transients on a Stewart platform, yet they still rely on computationally heavy analytical models and do not address the BEV/AV comfort envelope [14]. Recent observer-based control studies further highlight the relevance of robust estimation under uncertainty, disturbances and measurement noise. Although interval observers for switched nonlinear PDE systems and extended-state-observer-based control strategies for steer-by-wire systems are not ride-comfort methods, they support the need for bounded parameter estimation, disturbance-aware interpretation and quality screening when transient dynamic signals are used for subsequent comfort or control-oriented assessment [15,16].

To overcome these limitations, a short-time identification and reconstruction tool is developed to estimate the frequency, amplitude, and damping of a signal and thereby assess the impact of component modifications on comfort through simple, cost-effective transient tests performed on the real or virtual vehicle. By analysing real-world manoeuvres such as bump crossings or braking inputs, the methodology enables the identification of frequency, amplitude, and damping components that characterize the vehicle's dynamic response. Campbell diagrams are then used to visualize time frequency trends and highlight natural frequencies emerging within transient windows, linking identified components to comfort-relevant responses.

A central challenge is to isolate the frequency content of time-varying signals in the presence of brief events. Global, block-wise analyses tend to blur transient phenomena, whereas short-time, window-based processing exposes discrete mechanical or road-induced events relevant to comfort [8]. In this work, an adaptive windowing strategy is adopted: starting from a minimum window length, windows are adjusted to zero-crossing locations. This strategy provides sufficient temporal resolution to capture transients while improving the coherence of the subsequent parametric identification and reconstruction in each window [8,17,18].

The article is structured in three main parts. First, the methodology is introduced, and the comfort-weighting model is detailed. Second, the approach is validated on a synthetic test signal composed of 15 known components by reconstructing each window, computing the VDV, and quantifying the coherence. Finally, the same workflow is applied to three real-world transient road scenarios to demonstrate its performance under real road transient signals.

As a result, the methodology enables transient vibration responses to be decomposed into damped components and their contribution to comfort to be quantified on an event-by-event basis.

2. Method foundations

This section presents the methodological framework used to extract, reconstruct and evaluate the dominant vibration components of real-world transient road signals. The procedure combines an adaptive zero-crossing-based windowing, autoregressive (AR) spectral identification and a windowed numerical fitting stage using damped sinusoidal components, enabling the transient waveform to be reconstructed from physically interpretable frequency, amplitude and damping parameters. Building on the AR-based approach of Santos Arconada *et al.* [14], the present work extends the method in three directions: it accommodates more complex transient waveforms, improves the detection of dominant frequency components and refines their amplitude and damping through nonlinear fitting, and integrates a robust windowed fitting stage directly linked to ride-comfort metrics.

The overall workflow consists of four stages. First, the measured signal is pre-processed and segmented into individual transients by means of zero-crossing events with a positive local trend, and each segment is mapped to a well-defined adaptive analysis window. Second, an AR model is fitted to each window to obtain a compact spectral description and to identify the dominant damped frequency components. Third, these components are used as initial information for a nonlinear sinusoidal fitting procedure that refines amplitudes and damping ratios and reconstructs the transient response. Finally, the reconstructed time histories are screened using magnitude-squared coherence and post-processed to compute Vibration Dose Values in accordance with ISO 2631–1, providing a consistent basis for ride-comfort assessment.

2.1. Signal preprocessing (filtering and window segmentation)

The measured road signal is first low-pass filtered to attenuate high-frequency noise and small oscillations around zero that would otherwise generate spurious events. In all real-data applications considered in this article, an off-line fourth-order Butterworth low-pass filter with a cut-off frequency of 80 Hz is applied [19], implemented in zero phase by forward and reverse filtering and symmetric reflection padding at both ends of the signal [20]. This combination removes unwanted high-frequency content while preserving the timing and shape of the transients, which is essential for subsequent comfort-oriented vibration analysis [21].

The adaptive windowing strategy combines a nominal spectral-identification criterion with a practical zero-crossing-based segmentation procedure. In the present implementation, the AR-based PSD is evaluated on a frequency grid ten times finer than the basic FFT bin spacing used as numerical reference. Therefore, for a window of duration (T), the nominal FFT bin spacing is approximately $\Delta f_{FFT} = 1/T$, while the frequency grid used for AR-PSD peak localisation is approximated as $\Delta f_{GRID} = \Delta f_{FFT}/10 = 1/10T$. This grid refinement does not imply that the finite record has unlimited physical resolving power. Rather, it provides a dense evaluation grid for the parametric spectral model, allowing the dominant AR spectral peaks to be localised more accurately than with the raw FFT bin spacing. Based on a target grid spacing close to 0.1 Hz, the corresponding nominal window duration is approximately $T_{nom} \approx 1$ second. This nominal duration is not imposed as a fixed window length. It defines only the target duration used to search for the next suitable zero-crossing boundary.

Starting from the initial point of the current segment, all zero crossings of the filtered signal, including samples that lie very close to zero, are detected. Closely spaced crossings are then grouped and reduced to a single representative event. For each group, the local behaviour of the signal around the crossings is examined, and only those crossings that satisfy two conditions are retained: (i) the sample immediately before the crossing is non-positive, and (ii) the signal exhibits a net positive trend within a short time interval after the crossing. If several crossings meet these conditions within the same group, a single crossing is selected according to the local slope pattern, while the others are discarded. Among the admissible positive-slope zero-crossings located around the nominal duration, the crossing closest to T_{nom} is selected as the final boundary of the current window.

Therefore, the actual duration of each window, varies slightly according to the input signal, although it remains centred around the nominal duration used for spectral identification. The segmentation should therefore be understood as an adaptive zero-crossing procedure rather than as a fixed-duration windowing scheme. In addition, consecutive representative crossings that would define windows shorter than a user-defined minimum duration are merged or rejected, so that only segments longer than this minimum window length are kept for analysis. This minimum duration is not a second fixed window length, but a lower acceptance threshold introduced to avoid analysing very short zero-to-zero intervals that may result from local noise or small oscillations around equilibrium rather than from meaningful transient events. Such short windows provide insufficient time support for reliable AR parameter estimation and make the separation of close frequency components more sensitive to noise and model-order selection.

Therefore, the minimum window length acts as a lower bound that preserves enough spectral information while maintaining the temporal localisation needed to describe short-lived road transient events. This procedure removes spurious oscillations around zero while preserves the theoretical requirement of windows starting and ending at zero and ensures a stable set of onset markers and suitably long windows for transient definition [22,23].

For each accepted pair of consecutive zero crossings, the endpoints of the corresponding segment are finally adjusted so that the window starts and ends exactly at zero. This is done by locally interpolating between the boundary sample and its nearest neighbour. If a boundary sample (t_a, x_a) is followed by$(t_b, x_b)$and $x_a$and $x_b$have opposite signs, the zero-crossing time is estimated by linear interpolation as

$$t_0 = t_a - x_a\frac{t_b - t_a}{x_b - x_a}, \quad x_0 = 0\,. \tag{1}$$

The boundary sample is then replaced by $(t_0, 0)$ while the remaining samples of the segment are left unchanged. This local endpoint correction removes residual offsets at the window boundaries and yields windows that start and end at zero, which are well suited for the subsequent autoregressive analysis [24,25].

Each accepted segment is then resampled to a fixed length of $L = 2^N$ samples. In this work, $N = 10$ was used, resulting in $L = 1024$ samples per analysis window. This resampling step gives all windows the same numerical length after their adaptive physical duration has been defined. This fixed length provides a common numerical representation for all windows and keeps the AR-PSD evaluation procedure consistent across segments, while the physical duration of each window remains adaptively defined by the zero-crossing boundaries. Although the discrete Fourier transform can be evaluated for arbitrary record lengths, power-of-two lengths are computationally advantageous for FFT-based numerical operations [26]. The final endpoint of the current window is then used as the initial point of the following window, resulting in a sequential and non-overlapping adaptive segmentation of the transient response.

The sensitivity of the segmentation is mainly governed by the nominal window duration and the zero-crossing endpoint correction. Short windows improve temporal localisation but reduce the amount of data available for AR parameter estimation, making closely spaced components more sensitive to noise and model-order selection. Long windows improve spectral stability but may blur transient behaviour and weaken the local-stationarity assumption required for AR-based identification. Inaccurate endpoint correction may also introduce boundary discontinuities and spectral leakage. The selected strategy therefore provides a compromise between spectral discrimination, transient localisation and numerical repeatability across consecutive windows.

2.2. Frequency components identification through autoregressive model spectral analysis

Unlike a classical FFT-based periodogram, the frequency component identification in the proposed workflow relies on an autoregressive power spectral density estimate. Parametric autoregressive spectral estimators can provide higher apparent spectral resolution than classical non-parametric FFT-based estimators for short data records, provided that the analysed signal is adequately represented by the selected autoregressive model order [27,28]. This property makes AR-based spectral estimation particularly suitable for the identification of narrow spectral peaks in short transient windows.

Before estimating the spectral content, each transient window obtained is mapped onto an internal uniform time grid. For a given window j, the absolute time axis is shifted so that the transient starts at t = 0, and the window duration T_j is recorded. The signal is then represented on the fixed grid of $L = 2^N$ samples defined in Section 2.1 using shape-preserving cubic interpolation. This common representation provides a consistent numerical basis for the AR spectral estimation and for the comparison of frequency components across windows.

Autoregressive (AR) models provide a parametric description of a locally stationary time series in which each sample is expressed as a linear combination of past samples (M) plus a prediction error [29]. In practical terms, the AR model is used here to obtain a compact spectral representation of each short transient window before the nonlinear reconstruction stage. For a transient window of N uniformly sampled points

$$\ddot{x}(n) = \sum_{i=1}^{M} a_i\ddot{x}(n-1) + \ddot{e}(n), \tag{2}$$

where $\ddot{x}(n)$ is the current value of the signal, $a_i$are the AR coefficients (predictor weights), M is the model order that indicates the number of the past values used to predict the current value and $\ddot{e}(n)$ is the prediction error. The Autoregressive process can also be formulated in the z-domain for spectral analysis. The z-transform of the AR model is expressed as

$$X(z) = \sum_{i=1}^{M} a_i X(z)z^{-i} + E(z), \tag{3}$$

where *X(z)* is the z-transform of the signal and *E(z)* the z-transform of the predictive error. Reorganizing Eq. (3), leads to

$$X(z)\left(1 - \sum_{i=1}^{M} a_i z^{-i}\right) = E(z). \tag{4}$$

From Eq. (4) the AR synthesis filter transfer function in the z-domain is defined as the output-to-input ratio

$$H(z) = \frac{X(z)}{E(z)} = \frac{1}{1 - \sum_{i=1}^{M} a_i z^{-i}}. \tag{5}$$

The Power Spectral Density (PSD) of the AR process is obtained from the frequency response of the transfer function evaluated on the unit circle $z = e^{jw}$. This results in the following expression for the PSD

$$R\left(e^{j\omega_d}\right) = \left|H\left(e^{j\omega_d}\right)^2\right|\sigma_p^2 = \frac{\sigma_p^2}{\left|1 - \sum_{i=1}^{M} a_i e^{-jwi}\right|^2}, \tag{6}$$

where σ_p^2 is the variance of the prediction error$\varepsilon(n)$, and $H\left(e^{j\omega_d}\right)$ is the frequency response of the AR model evaluated at the angular frequency $\omega_d = 2\pi f_d$, where f_d is the damped natural frequency in hertz. For each transient window, the AR coefficients are collected in the vector $a = [a_1, \ldots, a_M]^T$. The model order M is selected by scanning a candidate range $[M_{\min}, M_{\max}]$ on a representative subset of windows. For each candidate order M, an AR(M) model is identified and the corresponding prediction-error variance $\sigma_p^2(M)$ is computed. An Akaike-type information criterion is then evaluated as

$$AkIC(M) = L\ln\left(\sigma_p^2\right) + 2M, \tag{7}$$

where L is the number of samples in the window. The order $\widehat{M}$ that minimizes AIC(M) is retained and subsequently used for all windows to ensure a consistent spectral resolution across the dataset [30].

In this application, the AR-based spectral analysis provides robust estimates of the dominant damped frequencies, even for short noisy transient windows [27,31]. In contrast, the amplitudes and damping ratios inferred directly from the AR poles show large bias and variability for the window lengths considered here, and do not reproduce the measured transient waveforms with sufficient accuracy [32–34]. Therefore, the AR model is used solely to obtain robust frequency estimates, while amplitudes and damping ratios are estimated in the nonlinear fitting stage described in Section 2.3 [35].

2.3. Amplitude and damping identification through non-linear sinusoidal fitting

In this stage, each transient window is approximated in the time domain by a sum of damped sinusoids. The model parameters are estimated via non-linear least-squares fitting, with the number of modes K_j and the initial values of the dominant frequencies and amplitudes informed by the AR-based spectral analysis described in Section 2.2. This stage refines the modal amplitudes, frequencies and damping ratios, allowing each transient window to be reconstructed from physically interpretable parameters.

For a given window j, defined on a relative time axis t, the measured acceleration signal $y_j(t)$ is approximated as

$$y_j(t) = \sum_{m=1}^{K_j} A_{j,m} e^{-\zeta_{j,m} w_{n,j,m} t} \sin\left(w_{d,j,m} t\right), \tag{8}$$

where K_j is the number of retained modes, $A_{j,m}$ is the modal amplitude, $\zeta_{j,m}$ is the damping ratio and $\omega_{d,j,m} = 2\pi f_{d,j,m}$ is the damped circular frequency associated with the m-th mode in window j. The corresponding natural frequency is obtained from the standard relation for underdamped single-degree-of-freedom systems $w_{n,j,m} = w_{d,j,m}\left(\sqrt{1-\zeta_{j,m}^2}\right)^{-1}, f_{n,j,m} = w_{n,j,m}(2\pi)^{-1}$ so that each fitted mode directly yields both a damped frequency $f_{d,j,m}$ and a natural frequency $f_{n,j,m}$ consistent with a second-order oscillator.

For each window j, the number of modes K_j is set equal to the number of significant spectral peaks detected in the AR-based PSD of Section 2.2. These peak frequencies provide the initial values $f_{d,j,m}^{(0)}$. The associated AR spectral magnitudes are used to construct consistent initial amplitudes $A_{j,m}^{(0)}$, while the damping ratios $\zeta_{j,m}$ are initialized with a predefined value $\zeta^{(0)}$ used only to start the optimization. All parameters are then refined by the non-linear fit.

Before fitting, the measured signal in window j is resampled on a uniform time grid $t_n \in [0, T_j]$ with a fixed time step $\Delta t = 10^{-3}$ seconds using shape-preserving cubic interpolation. This time-domain interpolation provides a consistent reference signal for the nonlinear fitting stage and preserves the transient peak shape required for accurate amplitude and damping estimation. This produces a reference vector $y_j^{\mathrm{ref}}(t_n)$ against which the parametric model $y_j\left(t; \mathrm{p}_j\right)$ is compared

$$J_j\left(p_j\right) = \sum_{n=1}^{N_j} \left[y_j^{ref}(t_n) - \widehat{y}_j(t_n; \mathrm{P}_j)\right]^2. \tag{9}$$

The optimization is performed under simple bound constraints that enforce physical plausibility and reduce parameter correlation. Amplitudes are constrained between zero and the maximum absolute value of the measured signal in the window; damped frequencies are restricted to lie in a neighbourhood of their AR-based initial values$f_{d,j,m} = f_{d,j,m}^{(0)} \pm \varepsilon, \varepsilon = \pm 0.3 f_{d,j,m}$here, and damping ratios are limited to the underdamped range $0 \le \zeta_{j,m} \le 0.3$. These bounds, together with the AR-based initialization, stabilize the fit and avoid unrealistic heavily damped modes.

Because the cost function $J_j$is non-convex and may contain several local minima, a multi-start fitting strategy is adopted. This means that the same fitting problem is solved several times using different optimisation routines, reducing the risk of retaining a solution associated with a local minimum. For each window, up to five optimization trials are carried out, combining constrained non-linear least-squares algorithms of Levenberg–Marquardt type [36], bounded Nelder–Mead simplex searches [37] and a global particle-swarm optimization (PSO) [38]. Levenberg–Marquardt algorithms is a standard tool for nonlinear least-squares curve fitting and is widely used in vibration and rotor-dynamic applications because it exploits the local quadratic structure of the cost function and converges rapidly when a reasonable initial guess is available [39,40]. Nelder–Mead is a derivative-free simplex method that is particularly attractive for noisy or mildly non-smooth objective functions and has been successfully applied to parameter identification in low signal-to-noise scenarios [41,42]. PSO is a population-based global optimizer that has proven effective for modal parameter identification and structural model updating in the presence of multiple local minima and strong measurement noise [43–45].

In the present work, all three solvers operate on the same model $\widehat{y}_j(t)$, with the same bounds and AR-based initial frequencies. Each algorithm produces a candidate parameter vector $\mathrm{p}_j^{(r)}$and a residual value $J_j\left(\mathrm{p}_j^{(r)}\right)$; the solution with the smallest residual is retained as the final set of modal parameters for that window. This multi-start, multi-algorithm strategy combines the fast local convergence of gradient-based solvers with the robustness of direct-search and population-based methods and yields stable modal amplitudes and damping ratios even for short, noisy road-induced transients. The resulting window-wise modal parameters and reconstructed waveforms are then used as the basis for the windowed VDV and coherence analyses described in Section 2.4.

2.4. Signal quality evaluation and comfort metrics

Once the transient signal has been reconstructed as a sum of damped sinusoids in each window, the reconstructed response is first evaluated in terms of spectral consistency before the comfort metrics are interpreted. This quality-control step is included to verify that the fitted components preserve the dominant spectral content of the corresponding measured transient.

To assess the quality of the reconstructed signal and ensure that VDV values are based on physically meaningful fits, each window is also evaluated using spectral coherence. In this work, coherence is used as a frequency-dependent indicator of reconstruction quality. Specifically, we compute the magnitude-squared coherence function $\gamma_j^2(f)$ between the pre-processed measured signal and its reconstructed counterpart, using standard cross-spectral estimators as in classical random-data analysis [46]. The coherence between two signals (x and y) is defined as

$$\gamma^2{}_j = \frac{\left|G_{xy,j}(f)\right|^2}{G_{xx,j}(f) G_{yy,j}(f)}, \tag{10}$$

where $G_{xy,j}(f)$ is the Cross Power Spectral Density (CPSD) of both signals (x and y for the given window j) which describes the shared frequency content between the measured and reconstructed signals, and $G_{xx,j}(f)$ and $G_{yy,j}(f)$ are the Power Spectral Density (PSDs) of x_j and y_j respectively. The coherence satisfies $0 \le \gamma_j^2(f) \le 1$, values close to 1 indicating that the reconstructed signal is strongly related to the measured signal at frequency f, while values close to 0 indicate a poor reconstruction in that frequency range [47].

For reconstruction-quality screening, the magnitude-squared coherence was averaged over the analysis band using the reference PSD as a weighting factor. This weighted formulation gives greater relevance to frequency regions where the original signal contains significant energy and avoids over-penalising low-energy bands where coherence values are less meaningful for the reconstructed response. The reconstructed signal itself corresponds to the complete pre-processed event response, whereas the coherence indicator used to support comfort-oriented interpretation was evaluated over the 0.5 to 80 Hz band, consistent with the acceleration-based assessment range of ISO 2631-1.

The weighted average coherence was used as a quality-screening indicator before interpreting the VDV values. Since magnitude-squared coherence ranges from 0 to 1, values close to unity indicate that the reconstructed signal preserves the spectral structure of the reference signal in the analysed band [47,48]. Therefore, windows with weighted average coherence equal to or above 0.90 were classified as highly reliable reconstructions. Values between 0.80 and 0.90 were considered acceptable but interpreted with caution. Values below 0.80

were flagged as low-confidence reconstructions. These thresholds were used as practical quality-screening criteria for interpretation and were not used to tune the fitting procedure.

After this quality-control step, the reconstructed signal is used to compute a frequency-weighted vibration dose value (VDV) consistent with ISO 2631-1 recommendations for ride-comfort assessment. The VDV was computed for all reconstructed windows. However, windows with weighted average coherence below 0.80 were retained in the analysis but interpreted as low-confidence cases when discussing the comfort results, because their reconstructed spectral content was not considered sufficiently consistent with the measured signal.

Additionally, the coefficient of determination R^2 was computed between the pre-processed measured signal and the reconstructed signal in each window as a direct measure of time-domain agreement between the pre-processed measured signal and the reconstructed signal. R^2 quantifies the proportion of the reference signal variance reproduced by the reconstruction and was used as a complementary indicator of reconstruction accuracy.

For comfort assessment, a frequency weighting $W_a(f)$ is applied that depends also on the measurement axis $(x, y, z, \Delta x, \Delta y, \Delta z)$ in line with ISO 2631-1 so that the method can be applied uniformly to different directions of whole-body vibration. In the present implementation, this weighting is applied to each identified amplitude corresponding to each reconstructed frequency component in window j, with damped frequency $f_{d,j,m}$ by a scalar factor $W_a\left(f_{d,jm}\right)$. The resulting weighted acceleration signal $a_{w,j}(t) = W_a\left(f_{d,jm}\right) * a(t)$ emphasizes the frequency band most relevant to comfort and then it is used to compute the vibration dose value for window j in the standard form

$$VDV_j = \left(\int_0^T {a_w}^4(t)dt \right)^{\frac{1}{4}}, \tag{11}$$

with units of $\mathrm{m\,s^{-1.75}}$. Because of the fourth-power integration, short windows containing large transients contribute disproportionately to VDV_j, which makes this metric well suited to quantify transient road excitations in ride-comfort studies [5,6,49,50]. Here, VDV is interpreted as an event-wise vibration dose rather than as a full-route exposure value. Its fourth-power formulation is particularly sensitive to high acceleration peaks, making it suitable for comparing the relative severity of isolated transient manoeuvres under controlled conditions. The reported values therefore represent event-severity indicators rather than complete-route exposure values. For longer driving scenarios, individual event contributions could be accumulated using the standard fourth-power VDV summation.

Finally, a Campbell-type diagram is constructed from the windowed spectra to visualize the evolution of the dominant vibration components along the manoeuvre. In this work, it is used as a time-frequency map of the transient response. For each transient window, the magnitude of the auto- or cross-spectral estimate is mapped onto a time–frequency plane using the window index as a proxy for time, yielding a colour map $|S(f, j)|$ as a function of frequency and window number. This representation, commonly used in rotating machinery and vehicle NVH analysis, is particularly useful to highlight frequency components that are only active in a subset of windows (e.g. local resonances or manoeuvre specific events) and to provide a compact overview of how comfort-relevant components in the 0–80 Hz range appear, shift and decay over successive windows, complementing the window-wise VDV and coherence metrics.

3. Methodology validation

To validate and illustrate the effectiveness of the proposed methodology, a synthetic test case is generated using a synthetic signal composed of 15 sinusoidal frequency components. These components cover a representative frequency range relevant for ride comfort analysis. Each component is precisely defined by its frequency, amplitude and damping factor.

The synthetic signal is processed using the same workflow described in Section 2, including low-pass filtering, zero-crossing based segmentation, AR spectral analysis, non-linear sinusoidal fitting and comfort evaluation via VDV (Z-axis). For each window, the identified parameters are used to reconstruct the signal, and the reconstructed response is compared directly with the original synthetic one.

Fig. 1 compares the original synthetic signal with the analysed and reconstructed responses. The upper plot shows the complete time history, illustrating the close agreement between the reconstructed and synthetic signals. The lower panel provides a zoom of the first transient window together with the identified spectral peaks plotted on a logarithmic scale. The first window was chosen for illustration, as it most clearly reveals all the relevant frequency components. The right panel reports the relative errors of the identified components (frequency, amplitude and damping ratio) for each component in this first window.

The comparison demonstrates the methodology's capability to accurately identify and reconstruct individual frequency components, affirming its suitability and robustness for analysing real-world transient ride comfort signals. The results for the first window show excellent accuracy in the identification of the frequency components, with signed relative errors below 0.5% for all targets and values tightly clustered around zero. Damping shows a higher dispersion than the other identified parameters, although the signed relative errors remain within 5% and are small for most components. Amplitude identification presents signed relative errors below 8%, with a slight tendency towards underestimation in several components. Since damping controls the exponential decay of each reconstructed component and amplitude defines its initial magnitude, uncertainties in both parameters can affect the effective amplitude envelope of the reconstructed signal and, consequently, the VDV obtained from the fourth-power integration of the weighted acceleration.

To assess the isolated effect of damping uncertainty, an additional sensitivity check was performed on the synthetic validation signal. In this check, all identified damping ratios were conservatively perturbed by ±5%, while the frequencies, amplitudes, window definition and VDV calculation procedure were kept unchanged. The resulting variation in the reconstructed VDV remained below 0.5% with respect to the nominal reconstructed signal. This indicates that, for the synthetic validation case, the isolated effect of the observed damping uncertainty on the final VDV estimate is limited. From a comparative analysis perspective, this value can be interpreted as a small uncertainty margin for VDV-based comparisons obtained with the proposed reconstruction procedure. Therefore, when the VDV difference between two events or design configurations is clearly larger than this margin, the resulting comfort comparison is expected to remain robust. Conversely, if two configurations produce nearly identical VDV values, this damping-related uncertainty should be considered before drawing a final design conclusion.

The slight amplitude underestimation observed in some components is mainly attributed to spectral leakage, finite-window effects and the zero-crossing-based definition of the transient windows. Since the fitting is performed on short non-stationary segments, part of the signal energy may be redistributed among neighbouring frequency components, leading to slight amplitude underestimation in some modes. In addition, amplitude and damping are partially coupled in the nonlinear fit. In this context, a slightly lower fitted amplitude can be partly offset by a slower decay rate, allowing the reconstructed component to preserve the overall waveform over the window even when the individual parameter estimates show small signed biases. This explains why the parameter-level amplitude bias does not necessarily translate into a comparable error in the reconstructed VDV.

Fig. 2 summarizes the window-wise validation metrics obtained for the synthetic signal. The left panel compares the synthetic and

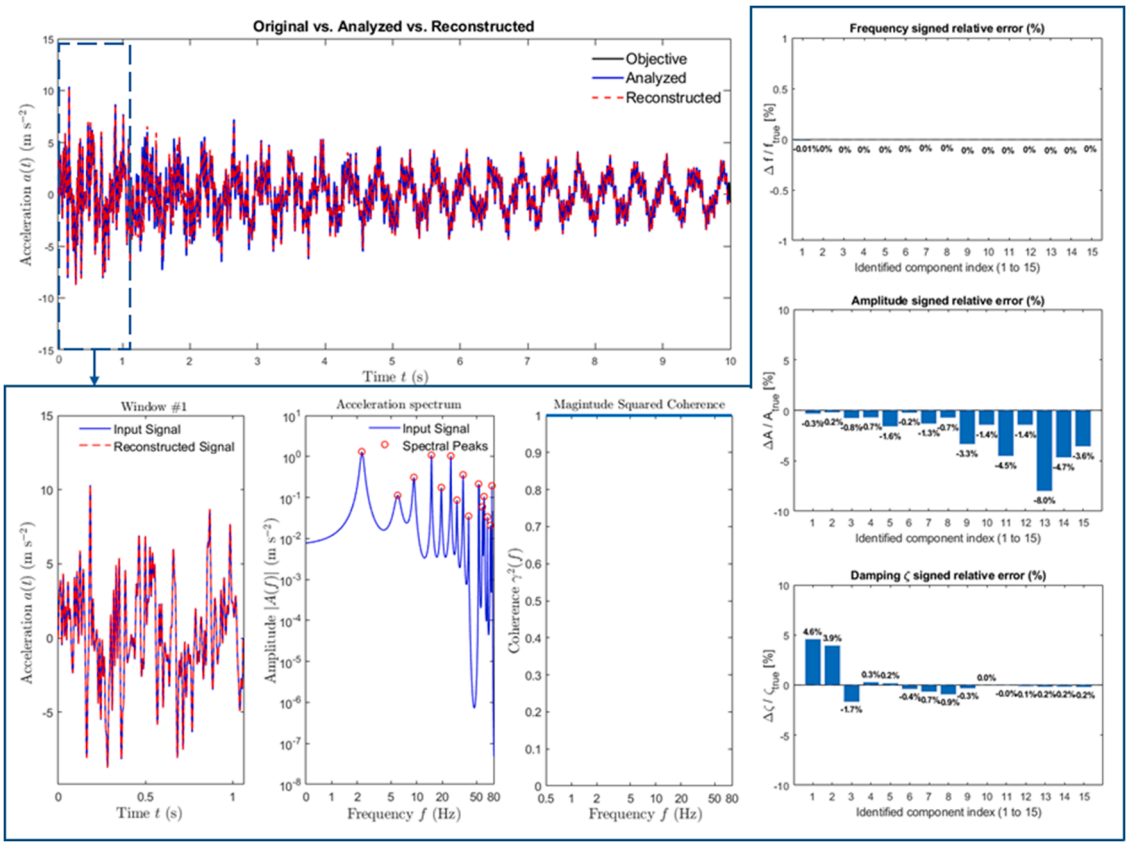


Fig. 1. Synthetic signal validation. Full signal reconstruction (time domain) and a detailed view of Window 1, including relative errors for frequency, amplitude and damping.

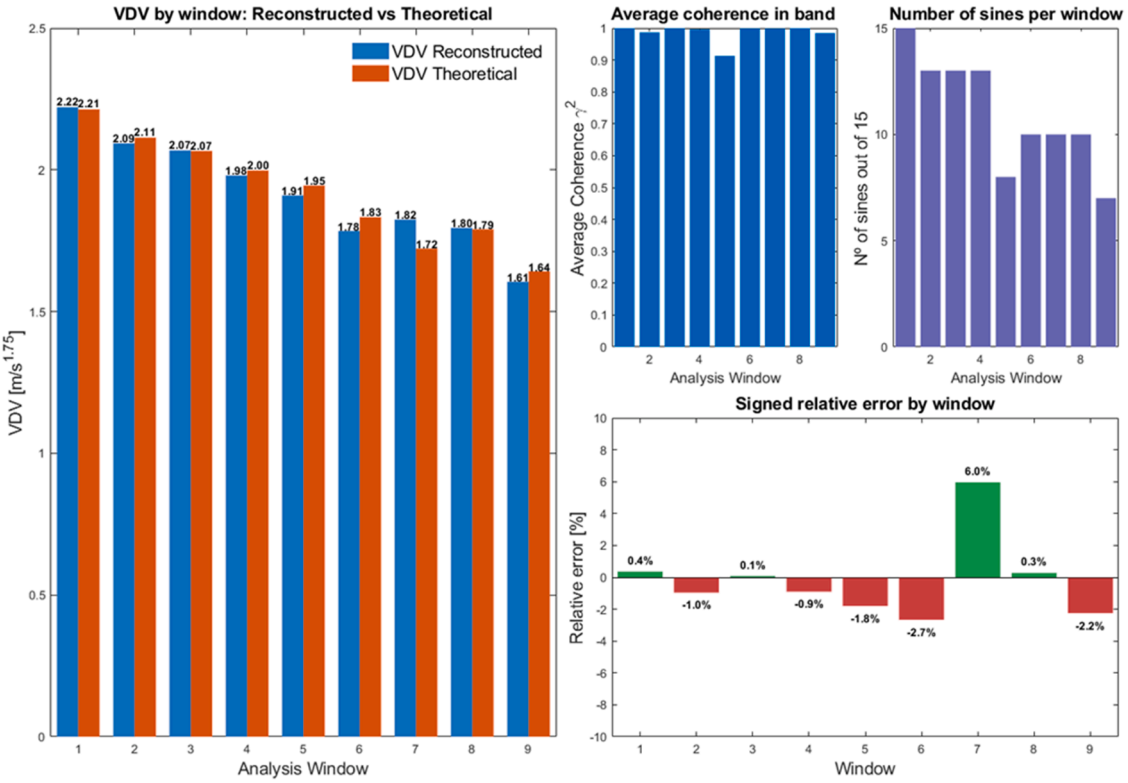


Fig. 2. Comfort metrics (VDV) and signal quality evaluation.

reconstructed VDV for each analysis window, while the top-right panels show, respectively, the average magnitude-squared coherence in the comfort band and the number of sinusoidal components effectively identified in each window. The bottom-right panel reports the signed relative error of the reconstructed VDV with respect to the synthetic value. As shown in Fig. 2, the reconstructed VDV errors remain small across the analysed windows, confirming that the combined frequency, amplitude and damping identification uncertainties have a limited effect on the final comfort metric.

Despite the progressive reduction in the number of identified components (Fig. 2 top-right graphic) due to the damping attenuation effect as the signal advances, the average coherence remains consistently close to unity in all windows, indicating that the reconstructed signals capture the relevant spectral content of the synthetic response. Consistently, the reconstructed VDV exhibits only small deviations from the synthetic values, with low signed relative errors across windows. This confirms that the proposed procedure is able to preserve the transient vibration dose while maintaining a high-quality match between measured and reconstructed signals, even when fewer modes are detected in later windows.

A Campbell diagram is finally plotted over all analysis windows to illustrate the ability of the method to track frequency components over time. This representation shows that, although some windows do not clearly exhibit every imposed component, the procedure consistently identifies and follows the dominant spectral features throughout the record (Fig. 3).

These analyses confirm that the methodology not only achieves precise identification and reconstruction of known frequency components but also reliably captures vibration dose metrics and tracks spectral content, validating its suitability for real-world ride comfort assessment as applied in Section 4.

R^2 quantifies the proportion of the signal variance reproduced by the reconstruction, while mean coherence evaluates whether the dominant spectral content is preserved within each window. The use of R^2 is appropriate because it provides a normalized measure of how well the reconstructed signal reproduces the variance of the reference signal [51]. In the present validation, all windows show R^2 values above 0.91, together with mean coherence values of at least 0.91, indicating that the reconstructed signal preserves both the dominant time-domain behaviour and the relevant spectral content before interpreting the corresponding VDV values (Table 1).

Campbell diagram frequency trends were interpreted only when the corresponding spectral bands appeared in windows classified as acceptable or highly reliable according to the coherence-based screening criterion. Persistent or recurrent bands across consecutive windows were considered physically meaningful trends, whereas isolated peaks located in low-energy or low-coherence regions were treated as low-confidence features and were not used to support comfort-related conclusions.

Overall, the synthetic validation shows that the method preserves the dominant spectral content and VDV trends across the analysed windows. Although Window 5 exhibits the lowest R^2 and mean coherence values, both metrics remain within an acceptable range, and the subsequent VDV discrepancy remains limited. This supports the suitability of the method for the real-world transient cases analysed in Section 4.

4. Application example using real world road transient signals

To assess the vehicle dynamic response under transient excitations, three experimental manoeuvres were performed: one-wheel bump impact, two-wheel bump impact, and brake input (Fig. 4). These manoeuvres were selected to excite distinct vibration modes such as heave, pitch and roll, associated with both suspended and unsuspended masses, ensuring a representative evaluation of the vertical and rotational dynamics relevant to ride comfort and stability [5]. The vehicle-fixed axes and sign convention follow ISO 8855 [52]. Accordingly, the analysis focuses on the centre-of-gravity degrees of freedom that best represent

Table 1
Window-wise R^2 accuracy and mean coherence metrics for the synthetic validation case.

Window	Mean coherence	R^2
1	0.99	0.999
2	0.98	0.985
3	0.99	0.999
4	0.99	0.998
5	0.91	0.912
6	0.99	0.997
7	0.99	0.992
8	0.99	0.999
9	0.98	0.996

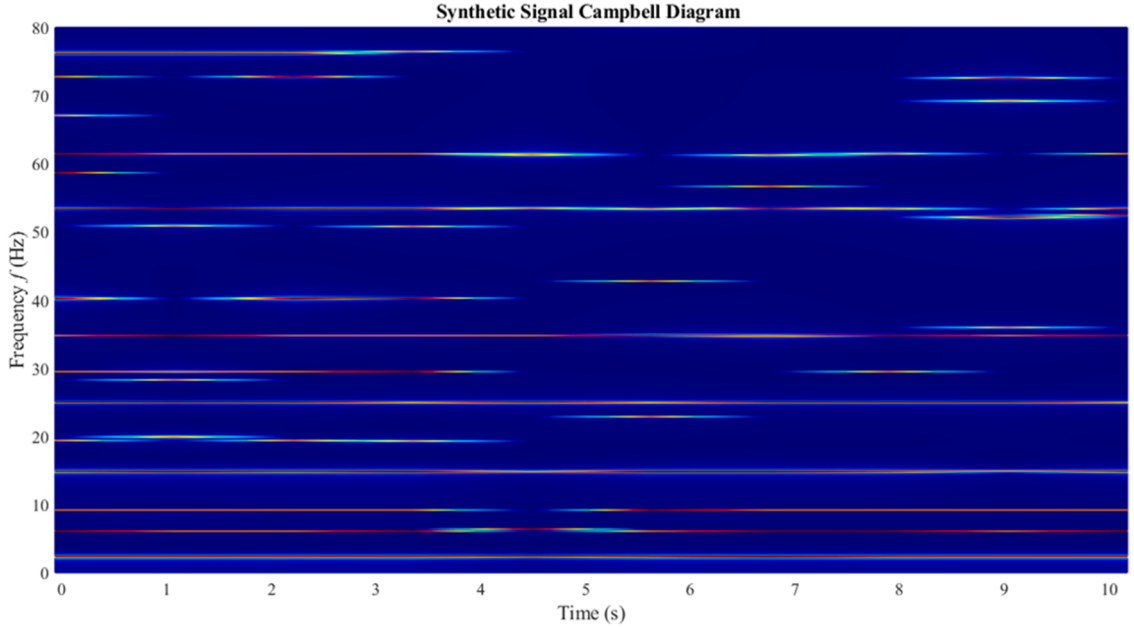


Fig. 3. Campbell Diagram of the synthetic reconstructed signal.

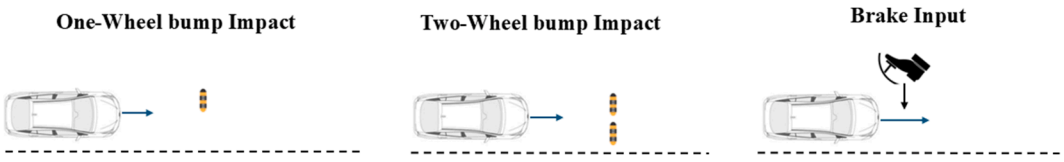


Fig. 4. Different Manoeuvres analysed.

each event: roll about x for the one-wheel bump, vertical acceleration along z for the two-wheel bump, and pitch about y for the brake input.

The dataset obtained from these three tests provides a diverse set of transient inputs capable of exciting the vehicle's natural frequencies, facilitating the validation of the proposed frequency reconstruction and identification methodology described in Section 3.

4.1. Experimental set-up

The tests had four tri-axial accelerometers TLD354C02 [53] mounted on the four vehicle corners (near each suspension mounting point) connected to a DAQ from Dewesoft. This configuration enables the capture of local vertical accelerations transmitted through the suspension system. The raw acceleration signals were then transformed to the vehicle's centre of gravity by applying rigid-body motion equations, allowing a global assessment of the vertical, pitch, and roll dynamics. This approach follows the methodology proposed by Santos Arconada et al. [14], which demonstrated that centre-of-mass transformation improves the consistency of components identification and allows a clearer comparison between experimental and simulation data. To ensure reproducibility and to clarify the boundary conditions of the experimental campaign, the vehicle configuration, instrumentation, test conditions and preprocessing settings used in the three manoeuvres are summarized in Table 2.

The main uncertainty sources in these tests are associated with vehicle speed repeatability, exact tyre-obstacle contact conditions, road surface variability, accelerometer alignment and sensor mounting stiffness, and the geometric assumptions used to transform the corner accelerations to the vehicle centre of gravity. Additional uncertainty may arise from filtering choices, event-window selection and the assumption of rigid-body motion between the measurement points and the centre of gravity. To reduce these effects, the tests were performed under the same dry-road condition and temperature, with fixed target speeds, identical sensor locations and the same preprocessing filtering and windowing parameters for all manoeuvres.

Table 2
Experimental setup and test conditions for the vehicle manoeuvres.

Item	Description
Test vehicle	Toyota Prius III Generation (2013) (FWD)
Vehicle loading condition	Driver (65 kg), Co-Pilot (70 kg), Instrumentation (4 kg)
Tyres	195/65/R15 Bridgestone T005 at 2.5 Bar (Front & Rear)
Environmental conditions	Dry asphalt test track; Ambient temperature: 20 °C. Asphalt temperature: 33 °C. Relative humidity: 65%
Manoeuvres	One-wheel bump impact, two-wheel bump impact and brake input
Number of repetitions	5 repetitions per manoeuvre
Target speed	10 km/h for bump tests; 15 km/h for brake input
Obstacle geometry	4.5 cm height, 30 cm width, 40 cm length
Sensors	Four TLD354C02 tri-axial accelerometers
Sensor location	Four vehicle corners, close to the suspension mounting points, following the coordinate layout reported in Santos Arconada et al. [14].
Sampling frequency	20 kHz
Reference system	Vehicle-fixed reference system according to ISO 8855 [52]
Analysed centre-of-gravity response	Roll about x for one-wheel bump, vertical acceleration along z for two-wheel bump and pitch about y for brake input

4.2. Experimental signal reconstruction through frequency component identification

Fig. 5 shows the measured acceleration signals obtained during the three manoeuvres. The response is clearly non-stationary, with short-duration transients embedded in longer intervals where the excitation level and the spectral content vary in time. Since the objective of this work is the analysis of road-induced transient events in a ride-comfort context, the subsequent results focus on the main event of each manoeuvre.

Prior to event extraction, the signals are low-pass filtered using the procedure described in Section 2.1. This step is required because the raw measurements contain spectral content outside the frequency range of interest for the present study. These out-of-band components do not contribute to the identification of the targeted vehicle dynamics. The filtered signals therefore provide a cleaner basis for selecting the transient interval and for the subsequent window-wise identification.

For each selected event interval, the results are presented in the same sequence for all tests. First, the reconstructed acceleration obtained from the identified damped sinusoids is compared against the original filtered signal within the event window. Second, the dominant spectral peaks used to initialize the reconstruction are reported by overlaying the spectral peaks identified from the AR-based spectral analysis on the spectrum of the measured acceleration. Third, the magnitude-squared coherence between the measured and reconstructed signals is evaluated over the frequency band of interest as the primary reconstruction-quality criterion, providing a quantitative assessment and confirming that the identified components explain the measured transient response.

4.3. One wheel bump impact

The one-wheel bump introduces an asymmetric vertical input that produces a roll-driven response at the vehicle centre of gravity; therefore, the rotation about the x axis is analysed. In this manoeuvre, the event response combines a forced contribution governed by the obstacle interaction and a subsequent free response phase (Fig. 6).

The reconstructed time history closely follows the measured transient over the event window. In the frequency domain, the identified peaks form a compact set in the low-frequency region and provide consistent initialization for the fitting stage. Reconstruction quality is supported by the magnitude-squared coherence, which remains high in the low-frequency range and decreases towards the upper end of the analysis band. In the frequency range relevant for comfort weighting on the rotational x axis according to ISO 2631-1 (up to 20 Hz), coherence remains particularly high, supporting the validation of the proposed method in the target band.

4.4. Two wheel bump impact

The two-wheel bump produces a largely symmetric excitation and therefore emphasizes the vertical centre of gravity response of the sprung mass, while also introducing additional short-lived components at higher frequencies. Compared with the one-wheel case, the event spectrum exhibits a richer set of peaks, and the reconstructed signal reproduces the measured transient with close agreement over the event window (Fig. 7).

Reconstruction quality is supported by the magnitude-squared coherence, which remains high over a broad portion of the analysis

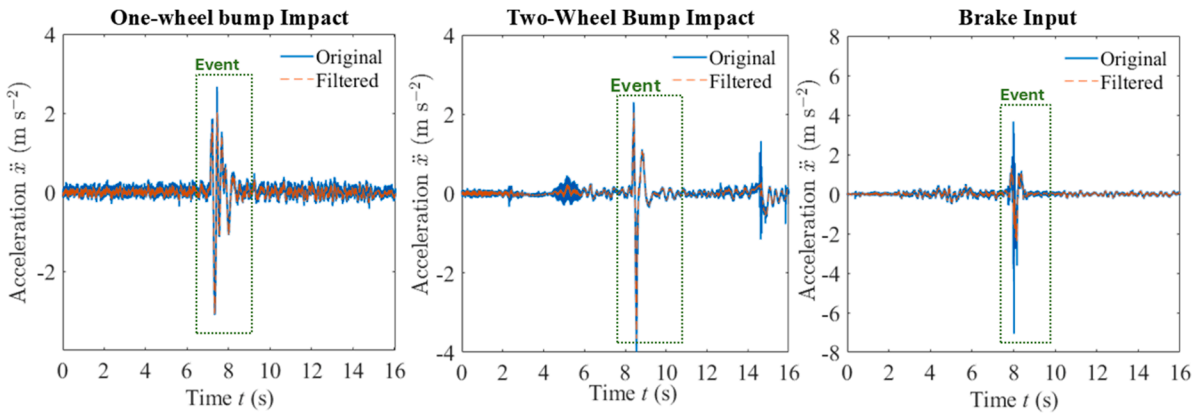


Fig. 5. Event Windows for each test. Original vs Filtered Signals.

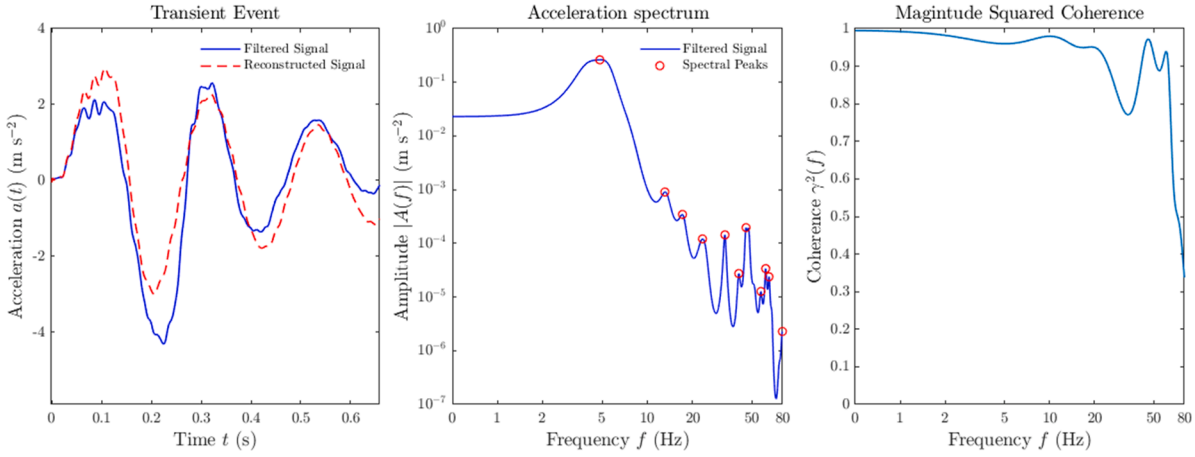


Fig. 6. One Wheel Bump Impact. ΔX Axis.

band. This indicates that the reconstruction preserves both the dominant low-frequency vertical response and the higher-frequency content present during the impact. Any local reductions in coherence are confined to frequency regions with low spectral amplitude and do not alter the dominant components that govern the event response.

4.5. Brake input

The brake input manoeuvre generates a transient that is dominated by pitch motion at the centre of gravity due to rapid load transfer. A dominant low-frequency component is identified, consistent with the pitch-dominated character of this event. The reconstructed signal follows the measured response over the event window, and the main spectral peaks observed in the measured event are retained in the reconstructed response, indicating that the identified components capture the governing dynamics of the transient (Fig. 8).

The magnitude-squared coherence remains above 0.8 up to 60 Hz, indicating a spectrally consistent reconstruction over most of the

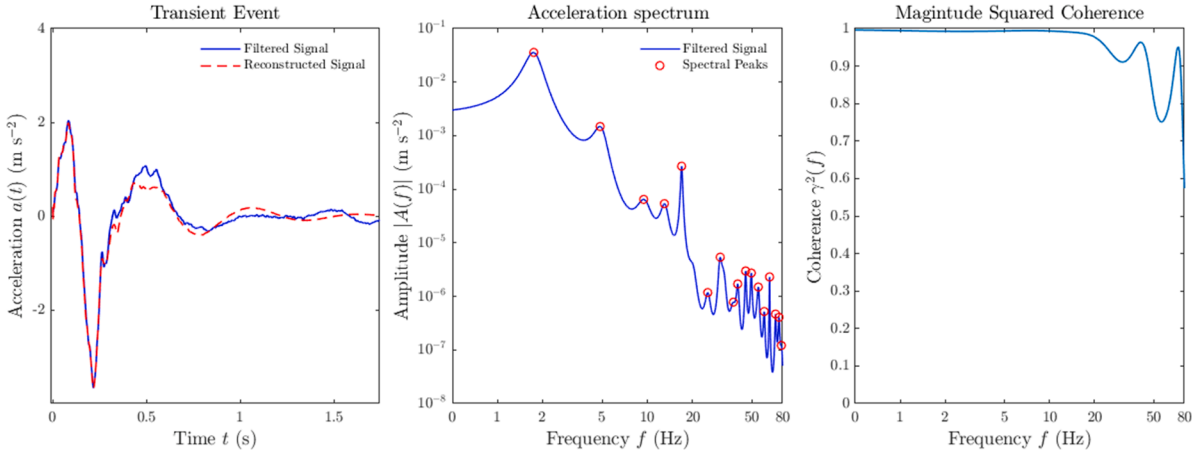


Fig. 7. Two Wheel Bump Impact. Z Axis.

analysis band. In the low-frequency region where the event concentrates most of its energy, coherence is particularly high, supporting the reliability of the reconstructed transient for subsequent comfort-weighted metrics.

4.6. Campbell diagram and comfort assessment (VDV)

For each reconstructed event, a Campbell-type time-frequency representation is displayed over the 0–80 Hz range to visualise the evolution of the spectral content during the transient event. The reconstructed response corresponds to the complete pre-processed event, while the comfort-oriented interpretation is restricted to the 0.5–80 Hz range, consistent with ISO 2631-1. The diagram highlights the dominant frequency bands activated by each manoeuvre and their time localisation within the event, offering a compact summary of the non-stationary response beyond a single-window view.

Fig. 9 compares the Campbell diagrams of the three manoeuvres over the displayed 0–80 Hz range, shown for the selected transient event interval together with the immediately following window. In all cases, the response is characterised by a small number of clearly defined frequency bands that remain visible across the event duration, with different relative prominence depending on the manoeuvre. The Campbell diagrams are used here as a compact diagnostic summary of the event spectral content, complementing the time-domain reconstructions and the coherence-based quality assessment. Comfort-oriented interpretation is addressed separately through the ISO comfort weighting.

The screening criteria described above were applied to the real manoeuvres before assigning physical meaning to the observed frequency bands. For example, in the brake-input case, the dominant low-frequency band was retained because it appears consistently during the selected event, agrees with the pitch-dominated time-domain response, and is located in a frequency region where the reconstruction coherence remains acceptable or high. Conversely, isolated traces appearing only in one window were not interpreted as physically meaningful unless they were supported by sufficient spectral energy and reconstruction coherence. In the present analysis, such isolated low-confidence traces were kept in the Campbell diagram for diagnostic completeness, but they were not used to support comfort-related conclusions or the VDV-based event ranking.

In parallel, the Vibration Dose Value (VDV) was calculated for the specific time window corresponding to the analysed event. This metric quantifies the accumulated vibration exposure experienced during the transient, serving as an indicator of ride comfort and perceived severity. By computing the VDV within the reconstructed event window, the analysis isolates the comfort impact directly attributable to the transient excitation, excluding steady-state conditions.

Table 3 reports the VDV obtained for each real-world event together with the corresponding R^2 between the filtered experimental signal and the reconstructed response. Here, R^2 is used as a reconstruction-quality indicator, quantifying how closely the reconstructed event reproduces the measured transient in the time domain. The obtained R^2 values, ranging from 0.835 to 0.967, support the interpretation of the corresponding VDV values.

The event-wise VDV values provide a direct numerical comparison of transient severity. In the present tests, the two-wheel bump reached 0.318 m $s^{-1.75}$ compared with 0.143 m $s^{-1.75}$ for the one-wheel bump and 0.171 m $s^{-1.75}$ for the brake input. Thus, the two-wheel bump generated approximately 2.2 times the vibration dose of the one-wheel bump and 1.9 times that of the brake-input event. These ratios are interpreted as relative event-wise comfort-severity indicators under the same ISO weighting and reconstruction procedure, rather than as absolute subjective comfort thresholds.

As a result, this methodology enables accurate calculation of the ride comfort of an experimental or numerical vehicle model through easy to implement individual transient road events. In addition, it allows the impact of structural changes in the vehicle model to be quantified in terms of comfort.

5. Results discussion

The proposed workflow was implemented as an offline analysis tool, prioritizing reconstruction accuracy and robustness over computational speed. This design choice is consistent with the objective of the present work, which is to identify transient frequency, amplitude and damping components and to compute comfort metrics with high fidelity, rather than to provide hard real time operation. The main computational cost is associated with the nonlinear fitting stage, especially when global optimization is used to avoid local minima. In contrast, filtering, adaptive windowing, AR-based spectral estimation, coherence calculation and VDV computation have a lower computational burden.

The method can be applied to longer signals because the analysis is performed window by window. Once the transient windows are defined, each segment can be processed independently, which makes the workflow suitable for batch processing and potential parallelization. The same principle applies to multi axis assessment: the user selects the axis or centre of gravity degree of freedom to be analysed, and the corresponding ISO 2631-1 weighting is applied before computing the VDV. Therefore, the framework is not restricted to a single signal direction, although the computational cost increases with the number of analysed axes, windows and retained frequency components.

Regarding noise robustness, the 80 Hz low pass filtering stage removes frequency content outside the selected comfort analysis band, while zero crossing selection, the minimum window duration and

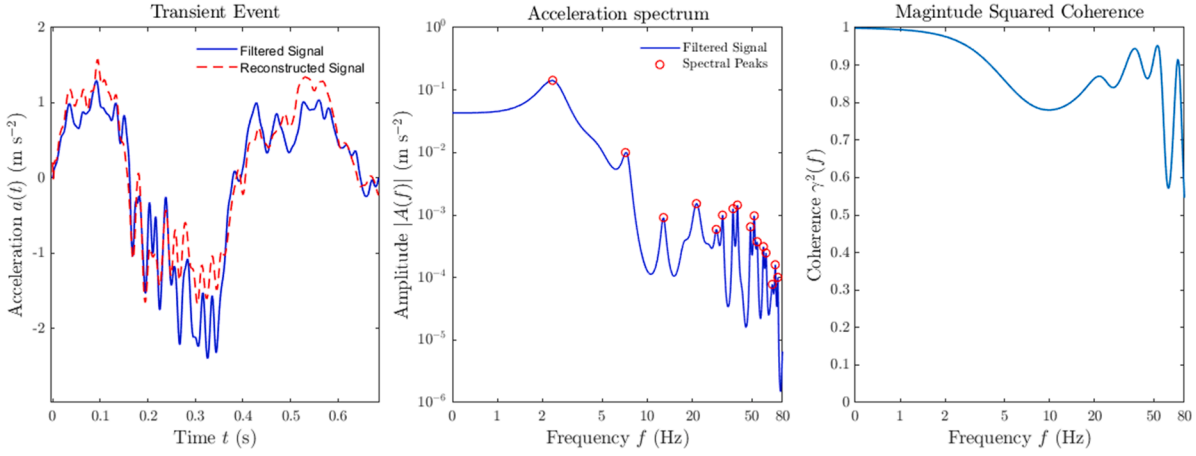


Fig. 8. Brake Input. ΔY Axis.

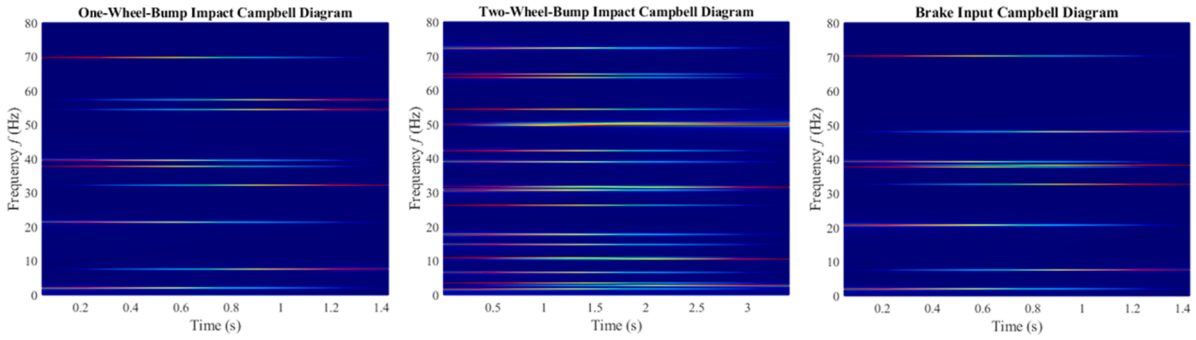


Fig. 9. Campbell Diagram for each event.

Table 3
VDV for each event.

	One bump Wheel impact	Two bump Wheel impact	Brake input
VDV Value (m $s^{-1.75}$)	0.143	0.318	0.171
R^2	0.835	0.967	0.896

coherence-based screening reduce the influence of spurious or poorly reconstructed windows. However, very low signal to noise ratios, weakly excited modes or closely spaced frequency components may still affect the reliability of amplitude and damping estimation. In addition, the present implementation is not intended for direct hard real time use because it relies on complete event windows, zero phase filtering and multi solver nonlinear optimization. A hard real time implementation would require further optimization of the existing functions, including causal filtering, faster event detection and simplified fitting routines, for example by reusing previous window estimates as initial conditions.

All numerical analyses were performed in MATLAB R2023a on a Windows 11 workstation equipped with an AMD Ryzen 7 7800 × 3D and 64 GB of RAM This information is provided only to document the computational environment used in the present offline implementation. As a practical reference, the complete analysis of a 15 s signal required approximately 3 min on this workstation, including filtering, adaptive segmentation, AR-based spectral analysis, nonlinear fitting, reconstruction-quality evaluation and VDV computation. The processing time depends mainly on the signal-to-noise ratio, the number of accepted windows, the number of identified components and the convergence behaviour of the nonlinear fitting stage.

6. Conclusion

This study demonstrates that transient road events can be analysed through a window-wise reconstruction framework without relying on global stationarity assumptions. The results show that decomposing short road-induced responses into damped sinusoidal components provides a traceable link between measured vibration signals, reconstruction quality and ISO 2631-1 comfort metrics. Unlike conventional block-wise spectral descriptions, the proposed approach preserves the temporal localisation of short events and enables their comfort contribution to be assessed individually. The main findings are summarised as follows.

- The synthetic validation confirms that the proposed identification and reconstruction chain can recover the transient spectral content with high accuracy at window level. For the tested signal, relative frequency errors remained below 0.5%, amplitude errors below 8%, and damping errors within 5%, while the reconstructed VDV closely matched the synthetic VDV across windows. High coherence values throughout the record demonstrate that accurate prediction can be achieved even when the number of detectable components decreases as the signal decays.
- For the experimental manoeuvres, the reconstructed event responses show close agreement with the measured transients in both time and frequency domains. Magnitude-squared coherence provides a transparent quality control metric: reconstructions remain spectrally consistent over most of the analysis band, and particularly high coherence is obtained in the frequency ranges most relevant for ISO comfort weighting for the analysed degrees of freedom. This supports the use of the reconstructed signals as a reliable basis for comfort metrics without requiring a detailed analytical vehicle model.
- Event-focused Campbell-type representations offer a compact diagnostic view of the dominant frequency bands active during each transient, complementing the time-domain reconstructions and coherence assessment. The event-wise VDV values enable a direct ranking of the analysed manoeuvres by comfort severity. In the present dataset, the two-wheel bump produced the largest dose (0.318), followed by brake input (0.171) and one-wheel bump (0.143), illustrating how the proposed workflow can quantify and compare the comfort impact of different transient excitations.

In closing, the proposed methodology provides a traceable route from real transient measurements to physically constrained reconstructions and event-wise comfort metrics, with window-wise coherence ensuring that conclusions are drawn only from spectrally meaningful fits. The results support its use in virtual development and experimental testing to assess the comfort impact of transient road events. Future work will apply this workflow to evaluate how structural modifications in different vehicle components affect transient vibration transmission and ride comfort, especially in BEV development, where reduced powertrain masking may make changes in chassis, suspension or drivetrain structural behaviour more perceptible to occupants.

CRediT authorship contribution statement

Oscar Montserrat Coll: Writing – original draft, Visualization, Validation, Software, Methodology, Investigation, Formal analysis, Conceptualization. **Jon García-Barruetabeña:** Writing – review & editing, Validation, Supervision, Methodology, Conceptualization.

Declaration of competing interest

The authors declare the following financial interests/personal relationships which may be considered as potential competing interests: Oscar Montserrat Coll reports financial support was provided by Fundación Automotive Intelligence Center. Oscar Montserrat Coll reports a relationship with Fundación Automotive Intelligence Center that includes: employment. If there are other authors, they declare that they have no known competing financial interests or personal relationships that could have appeared to influence the work reported in this paper.

Acknowledgments

The work presented in this paper has been carried out with the great support and the technological capabilities of AIC-Automotive Intelligence Center and University of Deusto.

Data availability

Data will be made available on request.

References

[1] J. Masri, M. Amer, S. Salman, M. Ismail, M. Elsisi, A survey of modern vehicle noise, vibration, and harshness: a state-of-the-art, Ain Shams Eng. J. 15 (2024) 102957, https://doi.org/10.1016/j.asej.2024.102957.
[2] C. Deubel, S. Ernst, G. Prokop, Objective evaluation methods of vehicle ride comfort—a literature review, J. Sound Vib. 548 (2023) 117515, https://doi.org/10.1016/J.JSV.2022.117515.
[3] S. Rana, Asaduzzaman, vibration based pavement roughness monitoring system using vehicle dynamics and smartphone with estimated vehicle parameters, Results Eng. 12 (2021) 100294, https://doi.org/10.1016/j.rineng.2021.100294.
[4] Guide to measurement and evaluation of human exposure to whole-body mechanical vibration and repeated shock, British Standards Institution, 1999.
[5] International Organization for Standardization, ISO 2631-1:1997 - Mechanical Vibration and Shock — Evaluation of Human Exposure to Whole-Body Vibration — Part 1: General requirements, Geneva, 1997. https://www.iso.org/standard/7612.html (accessed June 18, 2025).
[6] G.S. Paddan, M.J. Griffin, Evaluation of whole-body vibration in vehicles, J. Sound Vib. 253 (2002) 195–213, https://doi.org/10.1006/JSVI.2001.4256.
[7] C.-J. Kat, R.P. Gräbe, P. Jacobus Van Staden, T. Botha, P.S. Els, Difference thresholds for primary and secondary ride of a vehicle on a 4-poster test rig, Ergonomics 67 (2024) 1702–1714, https://doi.org/10.1080/00140139.2024.2349748.
[8] B. Zhang, C.A. Tan, T. Dai, Ride comfort and energy dissipation of vehicle suspension system under non-stationary random road excitation, J. Sound Vib. 511 (2021) 116347, https://doi.org/10.1016/J.JSV.2021.116347.
[9] Q. Sun, W.J. Yan, W.X. Ren, Analytical investigation into error propagation of power spectral density transmissibility (PSDT) based on coherence function, J. Sound Vib. 514 (2021) 116429, https://doi.org/10.1016/J.JSV.2021.116429.
[10] T. Sanders, G. Mavros, J. Knowles, Characterisation and generation of road surface roughness for improved tyre-road interaction models, Results Eng. 26 (2025) 105644, https://doi.org/10.1016/J.RINENG.2025.105644.
[11] S. Thanagasundram, S. Spurgeon, F. Soares Schlindwein, A fault detection tool using analysis from an autoregressive model pole trajectory, J. Sound Vib. 317 (2008) 975–993, https://doi.org/10.1016/J.JSV.2008.03.044.
[12] Y.M. Zhan, A.K.S. Jardine, Adaptive autoregressive modeling of non-stationary vibration signals under distinct gear states. Part 2: experimental analysis, J. Sound Vib. 286 (2005) 451–476, https://doi.org/10.1016/J.JSV.2004.10.023.
[13] V. Santos Arconada, J. García-Barruetabeña, Transient road signals simulation strategy in a Stewart platform, Mech. Based Des. Struct. Mach. 53 (2025) 1760–1777, https://doi.org/10.1080/15397734.2024.2394901.
[14] V.S. Arconada, J. García-Barruetabeña, R. Haas, Validation of a ride comfort simulation strategy on an electric Stewart Platform for real road driving applications, J. Low Freq. Noise Vib. Act. Control 42 (2023) 368–391, https://doi.org/10.1177/14613484221122109.
[15] Q. Shi, S. He, H. Wang, V. Stojanovic, K. Shi, W. Lv, Extended state observer based fractional order sliding mode control for steer-by-wire systems, IET Control Theory Appl. 18 (2024) 2287–2295, https://doi.org/10.1049/CTH2.12569.
[16] X. Song, Z. Peng, S. Song, V. Stojanovic, Interval observer design for unobservable switched nonlinear partial differential equation systems and its application, Int. J. Robust Nonlinear Control 34 (2024) 10990–11009, https://doi.org/10.1002/RNC.7553.
[17] J.B. Allen, L.R. Rabiner, A unified approach to short-time fourier analysis and synthesis, Proc. IEEE 65 (1977) 1558–1564, https://doi.org/10.1109/PROC.1977.10770.
[18] M. Festa, F. Stalter, A. Tavornmas, F. Gauterin, Human response to vehicle vibrations and acoustics during transient road excitations, Vibration 4 (2021) 357–368, https://doi.org/10.3390/VIBRATION4020023.
[19] S. Butterworth, On the theory of filter amplifiers, Exp. Wirel. Wirel. Eng. 7 (1930) 536–541.
[20] F. Gustafsson, Determining the initial states in forward-backward filtering, IEEE Trans. Signal Process. 44 (1996) 988–992, https://doi.org/10.1109/78.492552.
[21] A.V. Oppenheim, R.W. Schafer, J.R. Buck, Discrete Time Signal Processing, 2nd ed., Prentice Hall, Upper Saddle River, NJ, 1999.
[22] H.W. Shenton, L. Zhang, System identification based on the distribution of time between zero crossings, J. Sound Vib. 243 (2001) 577–589, https://doi.org/10.1006/JSVI.1999.3472.
[23] P.E. William, M.W. Hoffman, Identification of bearing faults using time domain zero-crossings, Mech. Syst. Signal Process. 25 (2011) 3078–3088, https://doi.org/10.1016/j.ymssp.2011.06.001.
[24] F.J. Harris, On the use of windows for harmonic analysis with the discrete fourier transform, Proc. IEEE 66 (1978) 51–83, https://doi.org/10.1109/PROC.1978.10837.
[25] National Instruments, Windowing Signals, 2026. https://www.ni.com/es/shop/data-acquisition/measurement-fundamentals/analog-fundamentals/understanding-ffts-and-windowing.html (accessed January 10, 2026).
[26] J.W. Cooley, J.W. Tukey, An algorithm for the machine calculation of complex fourier series, Math. Comput. 19 (1965) 297–301, https://doi.org/10.1090/S0025-5718-1965-0178586-1.
[27] S.M. Kay, S.L. Marple, Spectrum analysis—a modern perspective, Proc. IEEE 69 (1981) 1380–1419, https://doi.org/10.1109/PROC.1981.12184.
[28] S. Lawrence Marple Jr., Digital Spectral Analysis, 2nd ed., Dover Publications, Mineola, NY, 2019.
[29] Y.M. Zhan, A.K.S. Jardine, Adaptive autoregressive modeling of non-stationary vibration signals under distinct gear states. Part 1: modeling, J. Sound Vib. 286 (2005) 429–450, https://doi.org/10.1016/J.JSV.2004.10.024.
[30] H. Akaike, A new look at the statistical model identification, IEEE Trans. Autom. Contr. 19 (1974) 716–723, https://doi.org/10.1109/TAC.1974.1100705.
[31] M. Thomas, Operational modal analysis by short-time autoregressive modeling, in: 24th Seminar on Machinery Vibration, CMVA = ACVM, CMVA/ACVM, 2006. https://www.researchgate.net/publication/263256135_Operational_modal_analysis_by_short_time_autoregressive_modeling (accessed February 15, 2026).
[32] P.E. Gautier, C. Gontier, M. Smail, Robustness of an arma identification method for modal analysis of mechanical systems in the presence of noise, J. Sound Vib. 179 (1995) 227–242, https://doi.org/10.1006/jsvi.1995.0015.
[33] V.H. Vu, M. Thomas, Uncertainties on modal parameters by operational modal analysis, Mech. Ind. 15 (2014) 153–158, https://doi.org/10.1051/meca/2014018.
[34] M. Smail, M. Thomas, A. Lakis, ARMA models for modal analysis: effect of model orders and sampling frequency, Mech. Syst. Signal Process. 13 (1999) 925–941, https://doi.org/10.1006/mssp.1999.1235.
[35] T.P. Zieliński, K. Duda, Frequency and damping estimation methods: an overview, Metrol. Meas. Syst. 18 (2011) 505–528. www.metrology.pg.gda.pl (accessed February 15, 2026).
[36] J.J. Moré, The Levenberg-Marquardt algorithm: implementation and theory, (1978) 105–116. https://doi.org/10.1007/BFB0067700.
[37] M.J. Box, A new method of constrained optimization and a comparison with other methods, Comput. J. 8 (1965) 42–52, https://doi.org/10.1093/comjnl/8.1.42.
[38] J. Kennedy, R. Eberhart, Particle swarm optimization, in: Proceedings of IEEE International Conference on Neural Networks, Perth, 1995, pp. 1942–1948, https://doi.org/10.1109/ICNN.1995.488968.
[39] H.P. Gavin, The Levenberg-Marquardt Algorithm for Nonlinear Least Squares Curve-Fitting Problems, Durham, NC, 2024. https://people.duke.edu/~hpgavin/ce281/lm.pdf (accessed November 30, 2025).
[40] R. Rzadkowski, P. Troka, M. Kowalski, Nonsynchronous rotor blade vibrations in last stage of 380 MW LP steam turbine at various condenser pressures, Appl. Sci. 12 (2022) 4884, https://doi.org/10.3390/app12104884.
[41] A. Maia, E. Ferreira, M.C. Oliveira, L.F. Menezes, A. Andrade-Campos, Numerical optimization strategies for springback compensation in sheet metal forming, Comput. Methods Prod. Eng.: Res. Dev. (2017) 51–82, https://doi.org/10.1016/B978-0-85709-481-0.00003-3.
[42] C.C. Fuh, H.H. Tsai, Parameter identification using the nelder-mead simplex algorithm for low signal-to-noise ratio systems in a frequency domain, J. Mar. Sci. Technol. (Taiwan) 27 (2019) 332–342, https://doi.org/10.6119/JMST.201908_27(4).0004.
[43] M.A. Galewski, Spectrum-based modal parameters identification with particle swarm optimization, Mechatronics 37 (2016) 21–32, https://doi.org/10.1016/J.MECHATRONICS.2015.11.006.
[44] M. El-Kafafy, A. Elsawaf, B. Peeters, T. Vampola, P. Guillaume, Modal parameter identification using particle swarm optimization, Int. J. Syst. Appl. Eng. Dev. 9 (2015).
[45] K. Li, J. Fang, B. Sun, Y. Li, G. Cai, Structural dynamic model updating with automatic mode identification using particle swarm optimization, Appl. Sci. 12 (2022) 8958, https://doi.org/10.3390/APP12188958.
[46] J.S. Bendat, A.G. Piersol, Random data: analysis and measurement procedures: fourth edition. Random Data: Analysis and Measurement Procedures, 4th Edition, 2012, pp. 1–613, https://doi.org/10.1002/9781118032428.
[47] J.S. Bendat, A.G. Piersol, Random Data: Analysis and Measurement Procedures, 4th ed., Wiley, 2010.
[48] K. Shin, J.K. Hammond, Fundamentals of Signal Processing: For Sound and Vibration Engineers, Wiley, Chichester, 2008.
[49] M.J. Griffin, A comparison of standardized methods for predicting the hazards of whole-body vibration and repeated shocks, J. Sound Vib. 215 (1998) 883–914, https://doi.org/10.1006/JSVI.1998.1600.
[50] M.L.M. Duarte, P.A. de Araújo, F.C. Horta, S. Del Vecchio, L.A.P. de Carvalho, Correlation between weighted acceleration, vibration dose value and exposure time on whole body vibration comfort levels evaluation, Saf. Sci. 103 (2018) 218–224, https://doi.org/10.1016/J.SSCI.2017.11.008.
[51] D. Chicco, M.J. Warrens, G. Jurman, The coefficient of determination R-squared is more informative than SMAPE, MAE, MAPE, MSE and RMSE in regression analysis evaluation, PeerJ Comput. Sci. 7 (2021) e623, https://doi.org/10.7717/peerj-cs.623.
[52] International Organization for Standardization, ISO 8855:2011 - Road vehicles, Vehicle Dynamics and Road-Holding Ability, Vocabulary, Geneva, 2011. https://www.iso.org/standard/51180.html (accessed February 17, 2026).
[53] PCB Piezotronics, Model TLD354C02: Triaxial ICP Accelerometer, 2026. https://www.pcb.com/es/productos?m=tld354c02 (accessed May 19, 2026).